Article

Estimating Ground Level NO$_2$ Concentrations over Central-Eastern China Using a Satellite-Based Geographically and Temporally Weighted Regression Model

Kai Qin [1],*, Lanlan Rao [1], Jian Xu [2] (iD) **, Yang Bai [3],*, Jiaheng Zou [1], Nan Hao [4], Shenshen Li [5]** and **Chao Yu [5]**

[1] School of Environment Science and Spatial Informatics, China University of Mining and Technology, Xuzhou 221116, China; raolanlan2016@163.com (L.R.); zoujiaheng@cumt.edu.cn (J.Z.)

[2] German Aerospace Center (DLR), Remote Sensing Technology Institute, 82234 Weßling, Germany; jian.xu@dlr.de

[3] College of Environment and Planning, Henan University, Kaifeng 475001, China

[4] European Organization for the Exploitation of Meteorological Satellites, 64283 Darmstadt, Germany; Nan.Hao@eumetsat.int

[5] Institute of Remote Sensing and Digital Earth, Chinese Academy of Sciences, Beijing 100094, China; lishenshen@126.com (S.L.); yuchao@radi.ac.cn (C.Y.)

* Correspondence: qinkai20071014@163.com (K.Q.); baiyang_cumt@163.com (Y.B.); Tel.: +86-159-5066-3287 (K.Q.)

Abstract: People in central-eastern China are suffering from severe air pollution of nitrogen oxides. Top-down approaches have been widely applied to estimate the ground concentrations of NO$_2$ based on satellite data. In this paper, a one-year dataset of tropospheric NO$_2$ columns from the Ozone Monitoring Instrument (OMI) together with ambient monitoring station measurements and meteorological data from May 2013 to April 2014, are used to estimate the ground level NO$_2$. The mean values of OMI tropospheric NO$_2$ columns show significant geographical and seasonal variation when the ambient monitoring stations record a certain range. Hence, a geographically and temporally weighted regression (GTWR) model is introduced to treat the spatio-temporal non-stationarities between tropospheric-columnar and ground level NO$_2$. Cross-validations demonstrate that the GTWR model outperforms the ordinary least squares (OLS), the geographically weighted regression (GWR), and the temporally weighted regression (TWR), produces the highest R^2 (0.60) and the lowest values of root mean square error mean (RMSE), absolute difference (MAD), and mean absolute percentage error (MAPE). Our method is better than or comparable to the chemistry transport model method. The satellite-estimated spatial distribution of ground NO$_2$ shows a reasonable spatial pattern, with high annual mean values (>40 μg/m^3), mainly over southern Hebei, northern Henan, central Shandong, and southern Shaanxi. The values of population-weight NO$_2$ distinguish densely populated areas with high levels of human exposure from others.

Keywords: NO$_2$; ground level; OMI; GTWR; China

1. Introduction

High ground level nitrogen oxides (NO$_x$ = NO + NO$_2$) are identified to be deleterious to human health, including decreased lung function and an increased risk of respiratory symptoms [1,2]. In addition, NO$_x$ can also produce other photochemical pollutants like O$_3$ in photochemical reactions, and acts as a gaseous precursor of aerosols and acid rain. Thus, the NO$_x$ concentration has been

included in multi-pollutant health indices [3] and its monitoring with complete spatial coverage is needed for exposure assessment. Since 1995, a series of satellites sensors, e.g., the Global Ozone Monitoring Experiment (GOME), the Scanning Imaging Absorption Spectrometer for Atmospheric Cartography (SCIAMACHY), and the Ozone Monitoring Instrument (OMI) have been successfully used to retrieve vertical NO_2 columns [4–8]. A dramatic increase in tropospheric NO_2 columns was revealed by the GOME and SCIAMACHY observations over China [9–12], the world's largest developing country along with the fastest growing economy.

Given that the existing ambient monitoring stations are sparse and unevenly distributed, there is a growing interest in the top-down satellite approach to obtain timely map of the spatial variations of surface concentrations of NO_2. A close relationship between ground level NO_2 concentrations and satellite-retrieved tropospheric NO_2 columns is expected based on two facts: (1) ground level NO_2 accounts for the majority of tropospheric NO_2 columns since human activities are their main source; and (2) the short lifetime of near-surface NO_2 results in little transport, both vertically and horizontally [13]. Petritoli et al. [14] demonstrated a significant correlation between in situ NO_2 measurements and the GOME tropospheric NO_2 columns. Recently, satellite observations were combined with land use regression models to provide spatio-temporally resolved ambient NO_2 [15–17]. In addition, an approach proposed by Lamsal et al. [18] that combines the vertical profiles of NO_2 generated by the chemical transport model and satellite tropospheric NO_2 columns, has been widely used to estimate ground level NO_2 concentrations [19,20]. However, the emission inventories used for the model simulations are based on outdated statistical data about human activities. These model-based profiles may not capture the actual vertical distribution of NO_2, especially where anthropogenic NO_x emissions are undergoing rapid changes such as in China [21]. Kim et al. [22] estimated the surface NO_2 volume mixing ratio by using multiple regression models with OMI data.

In this study, a geographically and temporally weighted regression (GTWR) model is introduced to estimate the ground level NO_2 concentrations by using the OMI tropospheric NO_2 columns over central-eastern China. The GTWR model is adapted from the geographically weighted regression (GWR) model [23–26] by taking into account spatio-temporal non-stationarity, which has been proven to effectively establish the relation between satellite-retrieved aerosol optical depth and fine particulate matter ($PM_{2.5}$) [27,28]. Furthermore, population-weighted ground level NO_2 concentrations are calculated to evaluate population exposure levels in different regions.

2. Study Area and Data

2.1. Study Area

This study focuses on the central-eastern China with a geographic scope of 20°N–45°N and 105°E–124°E (major populated areas in China, see left panel in Figure 1). The study area covers 20 province-level administrative units in mainland China, including the regions of the North China Plain, Yangtze River Delta, and Pearl River Delta that are most polluted. 715 ambient monitoring stations are located in this study area (see the right panel in Figure 1).
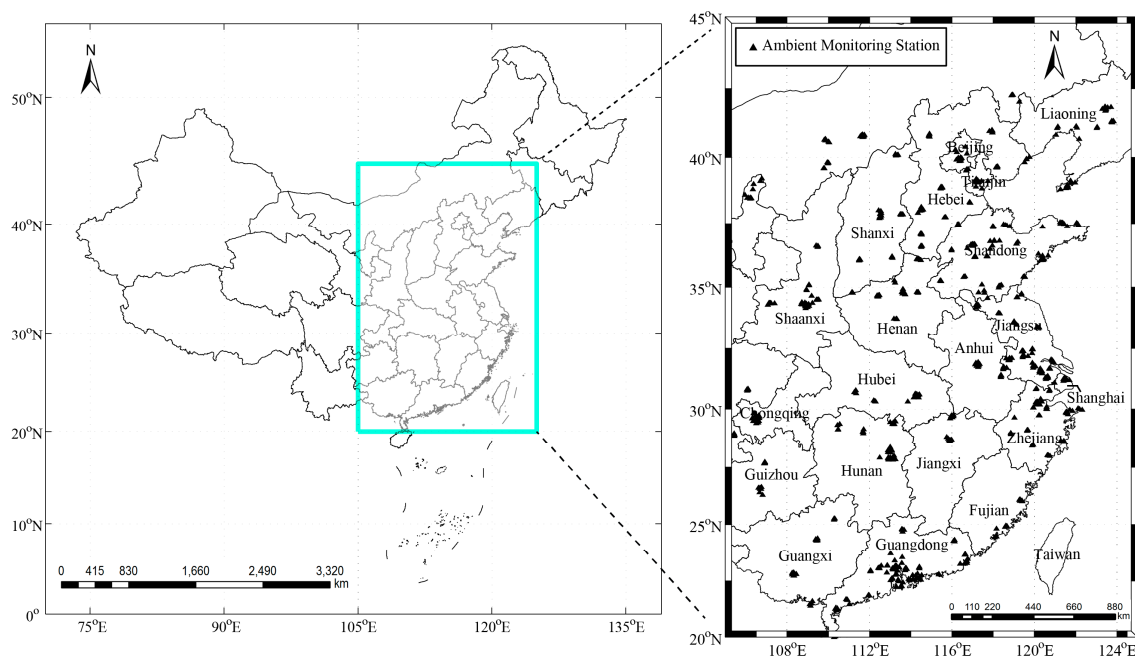
Figure 1. Study area and locations of ambient monitoring stations.

2.2. OMI Tropospheric NO₂ Columns

OMI is a Dutch-Finnish nadir-viewing hyperspectral instrument onboard the Earth Observing System Aura satellite in a Sun-synchronous orbit with an equatorial crossing time of approximately 13:45 local time. It measures sunlight backscattered radiances from the Earth in three channels covering a wavelength range of 270 to 500 nm (UV-1: 270 to 310 nm; UV-2: 310 to 365 nm; and, visible: 365 to 500 nm) at a spectral resolution of 0.45 to 0.63 nm [29]. OMI makes simultaneous measurements in a swath of width 2600 km, divided into 60 fields of view (FoVs). The FoVs vary in size from ~13 × 26 km near nadir to ~40 × 250 km at the outermost FoVs. The OMI measurements in the spectral range 402–465 nm are used to retrieve the NO₂ columns. First, NO₂ slant columns are determined from the OMI calibrated earthshine radiance spectra by using the differential optical absorption spectroscopy (DOAS) algorithm [30]. Second, the slant columns are then converted into the vertical columns using air mass factors (AMFs) calculated from radiative transfer models. Finally, the stratospheric and tropospheric column amounts are derived separately under the assumption that the two quantities are largely independent [31].

Here, we used the Version 3 Aura OMI NO₂ Standard Product (OMNO2) available from the NASA Goddard Earth Sciences Data and Information Services Center (http://disc.gsfc.nasa.gov/Aura/OMI/omno2_v003.shtml). The major improvements include: (1) an improved spectral fitting algorithm for retrieving slant column densities, including the use of monthly mean solar spectral irradiances; (2) improved Global Modeling Initiative model-based monthly a priori NO₂ and temperature profiles [32]. For further details, please refer to [33]. The main error sources in determining tropospheric NO₂ columns are associated with uncertainties in the surface albedo, aerosols, cloud interference, and the NO₂ vertical profile [34–37]. Overall, OMI retrievals tend to be lower in urban regions and higher in remote areas, but generally agree with other measurements within ±20% [38].

The data were filtered using a number of criteria [39] to ensure retrieval quality including: (1) cloud radiance fraction <0.3, (2) surface albedo <0.3, (3) solar zenith angles <85°, (4) 10 < cross-track positions < 50, and (5) root mean squared error of fit <0.0003. In addition, the cross track pixels affected by row anomaly (http://www.knmi.nl/omi/research/product/rowanomaly-background.php) were excluded, which was first noticed in the data in June 2007. Then, the NO₂ tropospheric column

densities from the Level-2 OMNO2 Swath product were binned on to a $0.1 \times 0.1°$ grid by calculating the area-weighted averages at each grid cell.

2.3. Ambient Monitoring Station Data

The Ministry of Environmental Protection of Republic of China has built 1497 ambient monitoring stations over 367 cities in order to assess the air quality in China. Hourly mean concentrations of air pollutants including $PM_{2.5}$, PM_{10}, NO_2, SO_2, and O_3 are available since 2013 in the national air quality publishing platform (http://106.37.208.233:20035/). In this study, hourly mean ground-based NO_2 concentrations of 715 stations in central-eastern China from 1 May 2013 to 30 April 2014 (13:00–15:00 local time) were included. The locations of these stations are shown in Figure 1.

2.4. Meteorological Data

In order to improve the performance of our regression model, a number of meteorological parameters such as air temperature, relative humidity, planetary boundary layer height, wind speed, and air pressure from the Weather Research & Forecasting Model (WRF, version 3.4.1) were used. NCEP FNL Operational Model Global Tropospheric Analyses dataset of $1 \times 1°$ resolution (http://rda.ucar.edu/dsszone/ds083.2/) was adopted in the WRF model. The WRF model is a mesoscale numerical weather prediction system designed for both atmospheric research and operational forecast, and serves as a wide range of meteorological applications across scales from tens of meters to thousands of kilometers. The nested domain scheme with 30 km horizontal grid space of WRF output centered at 115°E, 32.5°N was adopted, and the temporal resolution of WRF outputs was set 1 h intervals. The number of altitude levels is 30 and the top-level pressure is 50 hPa. The physical options used in WRF include the single-moment 3-class (WSM3) microphysics, the Yonsei University (YSU) PBL scheme, the Rapid Radiative Transfer Model (RRTM) longwave and Dudhia shortwave radiation schemes, and Noah land surface model. Then, the hourly mean meteorological data from 13:00 to 15:00 local time with a spatial resolution of 30 km was interpolated to a $0.1 \times 0.1°$ grid same as the NO_2 tropospheric column products.

2.5. Population Data

Worldwide gridded population data are available at 5-year intervals from 1995 to 2020 from the NASA Socioeconomic Data and Applications Center (Gridded Population of the World, v4; http://sedac.ciesin.columbia.edu/). The population data in 2013 was obtained by linearly-interpolating the data in 2010 and 2015 using $0.1 \times 0.1°$ resolution.

3. Methodology

3.1. GTWR Model

The GTWR model for the relationship of ground NO_2 concentrations and satellite tropospheric columns can be expressed as [40]:

$$NO_{2\_ground(i)} = \beta_0(u_i, v_i, t_i) + \beta_1(u_i, v_i, t_i)NO_{2\_Trop(i)} + \varepsilon_i, (i = 1, 2, \ldots, n) \quad (1)$$

where (u_i, v_i, t_i) represents the given coordinates of the training sample i in location (u_i, v_i) at time t_i. $NO_{2\_ground(i)}$ is the ground level NO_2 concentration observed by the ambient monitoring station at (u_i, v_i, t_i). $NO_{2\_Trop(i)}$ is the OMI NO_2 column density, $\beta_0(u_i, v_i, t_i)$ indicates the intercept of the GTWR model, $\beta_1(u_i, v_i, t_i)$ is a coefficient describing the unique spatial and temporal relationship between $NO_{2\_ground(i)}$ and $NO_{2\_Trop(i)}$. ε_i is the random error.

We introduced a number of meteorological parameters to the GTWR, i.e., air temperature at 2 m above the ground (T), relative humidity (RH), wind speed at 10 m above the ground (WS), planetary boundary layer height ($PBLH$), dew point temperature at 2 m above the ground (T_d), and the ambient

pressure near ground (*P*). Akaike's information criterion (AIC) [41] was used to judge whether the GTWR performance could be improved with the addition of each specific meteorological parameter. The *AIC* value for the GTWR model is expressed as:

$$AIC = 2n\ln(\hat{\sigma}) + n\ln(2\pi) + n\left(\frac{n + tr(\mathbf{S})}{n - 2 - tr(\mathbf{S})}\right) \tag{2}$$

where $\hat{\sigma}$ is the maximum likelihood estimation of the standard deviation for random error $\varepsilon_i (i = 1, 2, \ldots, n)$. $\mathbf{S}$ is the hat matrix of the dependent variable. $tr(\mathbf{S})$ is the trace of matrix $\mathbf{S}$. $\mathbf{S}$ and $\hat{\sigma}$ are calculated using Equations (17) and (18), respectively. The smaller *AIC* is, the better the model performance will be. As indicated in Table 1, the model performance improves substantially when the meteorological parameters of *PBLH, RH, WS, T*, and *P* are included. This is because that: (1) high temperature can increase photochemical reactions and hence reduce the lifetime of NO_2; (2) high relative humidity is related to low NO_2 concentration since it enhances the conversion rate of secondary aerosol from NO_X; (3) high *PBLH* is often related to low NO_2 concentration when it is supposed that NO_2 are well-mixed and confined within the planetary boundary layer; (4) high wind speed is favorable to pollutant dispersion that will result in the decrease of NO_2 concentration; and (5) high pressure increases atmospheric stability, leading to less atmospheric general circulation and thus more NO_2.

Table 1. Akaike's information criterion (AIC) values when satellite, planetary boundary layer height (PBLH), relative humidity (RH), wind speed at 10 m above the ground (WS), air temperature at 2 m above the ground (T), and ambient pressure near ground (P) data are included respectively in the geographically and temporally weighted regression (GTWR) model.

Satellite	PBLH	RH	WS	T	P
373,664	372,215	371,529	370,684	370,049	369,750

The GTWR can be modified as:

$$NO_{2\_ground(i)} = \beta_0(u_i, v_i, t_i) + \beta_1(u_i, v_i, t_i) \times NO_{2\_Trop(i)} + \beta_2(u_i, v_i, t_i) \times RH_{(i)} + \beta_3(u_i, v_i, t_i) \times T_{(i)}$$
$$+ \beta_4(u_i, v_i, t_i) \times PBLH_{(i)} + \beta_5(u_i, v_i, t_i) \times WS_{(i)} + \beta_6(u_i, v_i, t_i) \times P_{(i)} + \varepsilon_i, (i = 1, 2, \ldots, n) \tag{3}$$

$\beta_1(u_i, v_i, t_i), \beta_2(u_i, v_i, t_i), \beta_3(u_i, v_i, t_i), \beta_4(u_i, v_i, t_i), \beta_5(u_i, v_i, t_i)$, and $\beta_6(u_i, v_i, t_i)$ denote the slope of *T, RH, PBLH, WS*, and *P*, respectively. In the GTWR model, a local weighted least squares algorithm is employed to determine the parameters of $\beta(u_i, v_i, t_i)$:

$$\hat{\beta}(u_i, v_i, t_i) = (\mathbf{X}^T\mathbf{W}(u_i, v_i, t_i)\mathbf{X})^{-1}\mathbf{X}^T\mathbf{W}(u_i, v_i, t_i)\mathbf{Y} \tag{4}$$

where $\mathbf{W}(u_0, v_0, t_0)$ is a square matrix comprising the geographically and temporally weighted values of training datasets for measurement *i* by the diagonal elements. $\mathbf{X}$ and $\mathbf{Y}$ are, respectively, expressed as:

$$\mathbf{W}(u_0, v_0, t_0) = \begin{pmatrix} w_1(u_0, v_0, t_0) & 0 & \cdots & 0 \\ 0 & w_2(u_0, v_0, t_0) & \cdots & 0 \\ \vdots & \vdots & \ddots & \vdots \\ 0 & 0 & \cdots & w_n(u_0, v_0, t_0) \end{pmatrix} \tag{5}$$

$$\mathbf{X} = \begin{pmatrix} 1 & NO_{2\_Trop(1)} & RH_{(1)} & T_{(1)} & PBLH_{(1)} & WS_{(1)} & P_{(1)} \\ 1 & NO_{2\_Trop(2)} & RH_{(2)} & T_{(2)} & PBLH_{(2)} & WS_{(1)} & P_{(2)} \\ \vdots & \vdots & \vdots & \vdots & \vdots & \vdots & \vdots \\ 1 & NO_{2\_Trop(n)} & RH_{(n)} & T_{(n)} & PBLH_{(n)} & WS_{(1)} & P_{(n)} \end{pmatrix} \tag{6}$$

$$\mathbf{Y} = \begin{pmatrix} NO_{2\_ground(1)} \\ NO_{2\_ground(2)} \\ \vdots \\ NO_{2\_ground(n)} \end{pmatrix} \tag{7}$$

The temporal distance d_{i0}^t and the spatial distance d_{i0}^s are given by:

$$d_{i0}^t = |t_i - t_0| \tag{8}$$

$$d_{i0}^s = \sqrt{(u_i - u_0)^2 + (v_i - v_0)^2} \tag{9}$$

By combining the temporal distance d_{i0}^t and the spatial distance d_{i0}^s, the spatio-temporal distance is defined as:

$$d_{i0}^{st} = d_{i0}^s \otimes d_{i0}^t \tag{10}$$

where $\otimes$ denotes different kinds of operators. Here, the "+" operator is adopted, the d_{i0}^{st} is hence computed by:

$$d_{i0}^{st} = \lambda d_{i0}^s + \mu d_{i0}^t \tag{11}$$

where λ and μ stand for the scale factors of temporal and spatial distance, respectively. Furthermore, an ellipsoidal coordinate system is used to calculate the d_{i0}^{st}:

$$\begin{aligned} \left(d_{i0}^{st}\right)^2 &= \lambda \left(d_{i0}^s\right)^2 + \mu \left(d_{i0}^t\right)^2 \\ &= \lambda \left[(u_i - u_0)^2 + (v_i - v_0)^2\right] + \mu (t_i - t_0)^2 \end{aligned} \tag{12}$$

Gaussian distance decay-based functions and Euclidean distance are chosen to construct the spatio-temporal weight matrix $\mathbf{W}(u_0, v_0, t_0)$. The diagonal element $w_i(u_0, v_0, t_0)$ of the $\mathbf{W}(u_0, v_0, t_0)$ can be obtained by:

$$\begin{aligned} w_i(u_0, v_0, t_0) &= \exp\left[-\frac{1}{2}\left(\frac{d_{0i}}{h_{ST}}\right)^2\right], i = 1, 2, 3, \ldots, n \\ &= \exp\left\{-\frac{1}{2}\left(\frac{\lambda\left[(u_i - u_0)^2 + (v_i - v_0)^2\right] + \mu(t_i - t_0^2)}{h_{ST}^2}\right)\right\} \\ &= \exp\left\{-\frac{1}{2}\left(\frac{\left(d_{i0}^S\right)^2}{h_S^2} + \frac{\left(d_{i0}^T\right)^2}{h_T^2}\right)\right\} \\ &= \exp\left\{-\frac{1}{2}\frac{\left(d_{i0}^S\right)^2}{h_S^2}\right\} \times \exp\left\{-\frac{1}{2}\frac{\left(d_{i0}^T\right)^2}{h_T^2}\right\} \end{aligned} \tag{13}$$

where h_{ST}, h_T and h_S are the parameters of spatio-temporal, spatial, and temporal bandwidths, respectively.

Adaptive spatio-temporal bandwidths are adopted according to the density of sample points around the given point (u_0, v_0, t_0). When many sample points are closely distributed around the given point, the bandwidths are small. On the contrary, if there are not enough sample points near it, the bandwidths are larger when THE sample points are sparsely distributed. In practice, the bandwidths are determined with an optimization technique by cross-validation through minimizing Equation (14).

$$\mathrm{CV}(h_{ST}) = \sum_i (y_i - \hat{y}(h_{ST}))^2 \tag{14}$$

where the function $\hat{y}_i(h_{ST})$ denotes the predicted value from the GTWR which is built without sample i.

The ground level NO_2 at (u_i, v_i, t_i) is estimated by:

$$\hat{NO}_{2\_ground(i)} = \mathbf{x}_i^T \left(\mathbf{X}^T \mathbf{W}(u_i, v_i, t_i)\mathbf{X}\right)^{-1} \mathbf{X}^T \mathbf{W}(u_i, v_i, t_i)\mathbf{Y} \tag{15}$$

where $\mathbf{x}_i^T = \begin{pmatrix} 1, & NO_{2\_Trop(i)} & ,RH_{(i)} & ,T_{(i)} & ,PBLH_{(i)} & ,WS_{(i)} & ,P_{(i)} \end{pmatrix}$, and

$$\hat{\mathbf{Y}} = \begin{pmatrix} \hat{NO}_{2\_ground(1)} \\ \hat{NO}_{2\_ground(2)} \\ \vdots \\ \hat{NO}_{2\_ground(i)} \end{pmatrix} = \begin{pmatrix} \mathbf{x}_i^T (\mathbf{X}^T \mathbf{W}(u_i, v_i, t_i) \mathbf{X})^{-1} \mathbf{X}^T \mathbf{W}(u_i, v_i, t_i) \mathbf{Y} \\ \mathbf{x}_i^T (\mathbf{X}^T \mathbf{W}(u_i, v_i, t_i) \mathbf{X})^{-1} \mathbf{X}^T \mathbf{W}(u_i, v_i, t_i) \mathbf{Y} \\ \vdots \\ \mathbf{x}_i^T (\mathbf{X}^T \mathbf{W}(u_i, v_i, t_i) \mathbf{X})^{-1} \mathbf{X}^T \mathbf{W}(u_i, v_i, t_i) \mathbf{Y} \end{pmatrix} = \mathbf{SY} \qquad (16)$$

where **S** is the hat matrix of **Y** and is calculated as:

$$\mathbf{S} = \begin{pmatrix} \mathbf{x}_i^T (\mathbf{X}^T \mathbf{W}(u_i, v_i, t_i) \mathbf{X})^{-1} \mathbf{X}^T \mathbf{W}(u_i, v_i, t_i) \\ \mathbf{x}_i^T (\mathbf{X}^T \mathbf{W}(u_i, v_i, t_i) \mathbf{X})^{-1} \mathbf{X}^T \mathbf{W}(u_i, v_i, t_i) \\ \vdots \\ \mathbf{x}_i^T (\mathbf{X}^T \mathbf{W}(u_i, v_i, t_i) \mathbf{X})^{-1} \mathbf{X}^T \mathbf{W}(u_i, v_i, t_i) \end{pmatrix} \qquad (17)$$

The maximum likelihood estimation of the standard deviation for rand error is calculated as:

$$\hat{\sigma} = \sqrt{\frac{RSS}{n - tr(\mathbf{S})}} \qquad (18)$$

where *RSS* is the residual sum of squares between estimated ground level NO_2 concentrations and observed ones:

$$RSS = \mathbf{Y}^T (\mathbf{I_n} - \mathbf{S})^T (\mathbf{I_n} - \mathbf{S}) \mathbf{Y} \qquad (19)$$

3.2. Population-Weighted NO₂

The population data are introduced to calculate the population-weighted NO_2 (PNO_2) for different province-level administrative units:

$$PNO_2^j = \frac{\sum\limits_{k=1}^{m} NO_2^{j,k} \times Population^{j,k}}{\sum\limits_{k=1}^{m} Population^{j,k}} \qquad (20)$$

where PNO_2^j is the population-weighted NO_2 for province j, $NO_2^{j,k}$ and $Population^{j,k}$ are the NO_2 concentration and population data of pixel k in province j respectively.

3.3. Implementation Process and Statistical Indicators

To correlate the ground-based measurements with satellite data, the 715 ambient monitoring stations in the central-eastern China were merged into 509 stations by averaging all of the measurements within a grid of $0.1 \times 0.1°$. For the 509 grid cells, the total numbers of satellites and ambient monitoring observations are 54,867 (Figure 2a) and 110,545 (Figure 2b), respectively. Combining the satellite and ground observations, there are 31,463 valid data pairs (Figure 2c). The spatial distribution of the numbers of filtered satellite observations in Figure 2a shows a north-south difference, which is likely due to a higher cloud fraction over southern China. These 509 stations with total 31,463 dataset were divided randomly into 10 groups. The model fitting and cross-validation process was repeated 10 times, for every time one group was used for the cross-validation and the rest were used to train the fitting model until all groups were entered into the cross-validation once, thereby creating out-of-sample predictions for all the stations [42]. To be more specific, all of the 31,463 datasets were used both in the fitting and the cross-validation.

Some statistical indicators were employed to quantitatively assess the model performances. They are the coefficient of determination (R^2), whose higher value indicating better fitting accuracy, the root

mean square error (RSME), that is sensitive to both systematic and random errors, the mean absolute difference (MAD), that measures the mean error magnitude, and the mean absolute percentage error (MAPE), which characterizes the prediction accuracy of a statistical model.
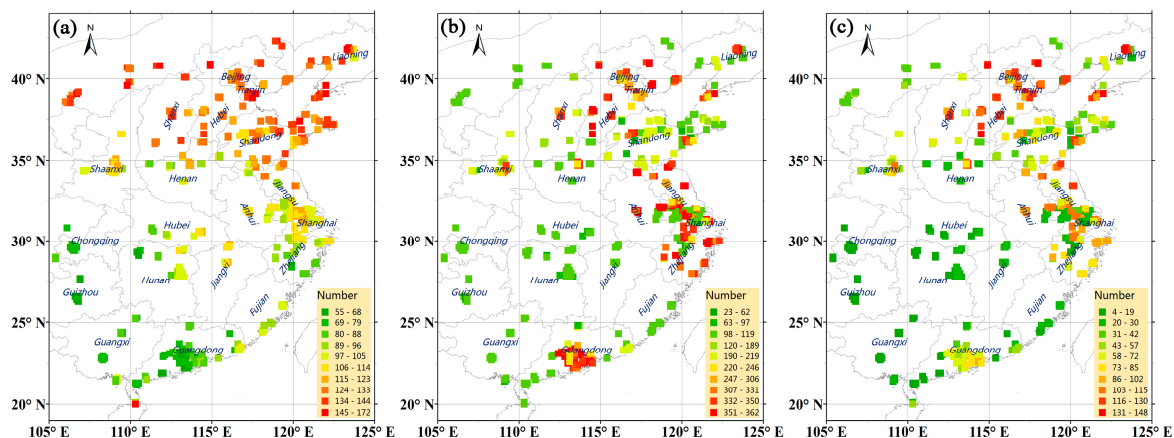

Figure 2. Numbers of satellite observations (**a**), ambient monitoring observations (**b**), and valid satellite and ground observation pairs (**c**) for 593 grid cells.

4. Results and Discussion

4.1. Spatio-Temporal Non-Stationarities between Tropospheric-Columnar and Ground Level NO$_2$

According to previous studies [43,44], the tropospheric NO$_2$ profiles show a large spatial-temporal variation. It is necessary to assess the impact of the spatio-temporal non-stationarities on the satellite-estimated ground level NO$_2$ concentrations. Lamsal et al. [38] showed that OMI retrievals are underestimated in urban regions and overestimated in remote areas about 20%. To isolate the influence of different land covers types, 293 pure urban grids and corresponding ambient stations were picked out from the total 509 grids and stations. As shown in Figure 3a, the mean values of tropospheric-columnar and corresponding ground level NO$_2$ over three provinces in eastern China (see also Figure 1) i.e., Shandong, Zhejiang, and Hunan, are compared. The mean values of OMI tropospheric NO$_2$ columns of the three provinces are different when the column data is composited with respect to the ground level NO$_2$ mass concentrations from ambient monitoring stations. This is related to the spatial difference in tropospheric NO$_2$ profiles due to different topographies and meteorological conditions. Moreover, the mean values of OMI tropospheric NO$_2$ columns in summer (May to July 2013), autumn (August to October 2013), winter (November 2013 to January 2014), and spring (February to April 2014) are compared in Figure 3b. The relationship between the NO$_2$ columns and ground level NO$_2$ shows a significant seasonal variation. The NO$_2$ columns in winter and autumn are higher than those in summer and spring when the values of ground level NO$_2$ are at the same level. This seasonal difference is more notable when ground concentrations increase, which is likely because of the longer lifetime of NO$_2$ in winter and autumn as compared to that in summer and spring. Consequently, it can exist for a longer time in the upper layer in the case of high ground emissions. The numbers of satellite observations used in Figure 3a,b are given in Tables 2 and 3, respectively. It should be pointed out that the numbers of satellite observations for high ground level NO$_2$ (>100 μg/m^3) are less than five in Hunan and in summer.

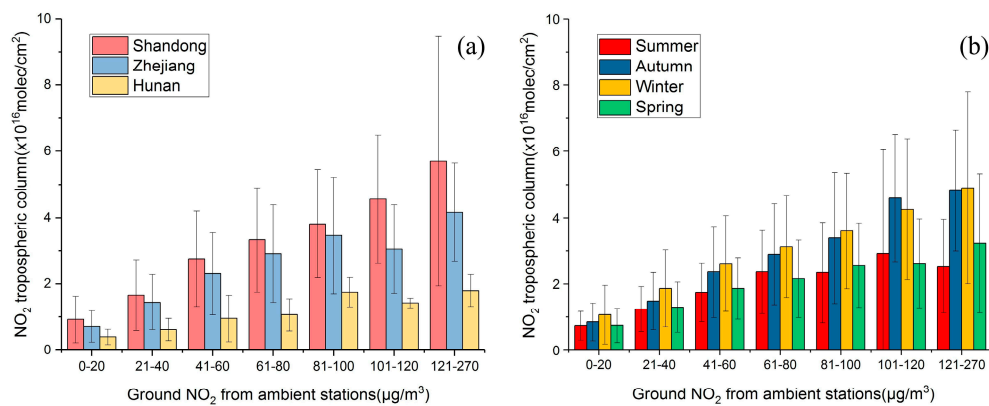**Figure 3.** Mean values of tropospheric NO$_2$ columns ($\times 10^{16}$ molec/cm^2) in different provinces (**a**) and different seasons (**b**) when the column data is composited with respect to the ground level NO$_2$ mass concentrations observed at 293 pure urban ambient monitoring stations. Error bars stand for one standard deviation.

Table 2. Numbers of satellite observations used in Figure 3a.

Province	Ground Level NO$_2$ Mass Concentrations						
	0–20	**21–40**	**41–60**	**61–80**	**81–100**	**101–120**	**121–270**
Shandong	1002	1265	611	299	126	68	79
Zhejiang	1371	1240	491	156	57	37	33
Hunan	66	101	57	24	13	3	2

Table 3. Numbers of satellite observations used in Figure 3b.

Season	Ground Level NO$_2$ Mass Concentrations						
	0–20	**21–40**	**41–60**	**61–80**	**81–100**	**101–120**	**121–270**
Summer	1567	1137	283	94	23	3	4
Autumn	1815	1423	436	169	51	21	13
Winter	1059	1785	1248	653	313	174	175
Spring	2022	2336	870	296	96	37	30

### 4.2. Comparison between Model Fitted and Ground-Observed NO$_2$

The ordinary least squares (OLS), GWR, temporally weighted regression (TWR), and GTWR models were tested using the same datasets. As shown in Tables 4 and 5, the OLS performance reveals that the tropospheric NO$_2$ columns are potentially useful for ground level NO$_2$ with R^2 of 0.45 and 0.44 for fitting and validation, respectively. The TWR outperforms the GWR with significant increases of R^2 values from 0.55 and 0.49 to 0.61 and 0.55. This suggests that the temporal non-stationarity is more dominant than the spatial non-stationarity between the tropospheric NO$_2$ columns and ground level NO$_2$. Among the four models, the GTWR has the best performance in both model-fitting and cross-validation with the highest R^2 and lowest errors (RMSE, MAD, and MAPE). Nevertheless, the GTWR regression shows a slight over-fitting, i.e., the R^2 generated from the cross-validation is 0.09 smaller than that from the model-fitting. In addition, the scatter plots in Figure 4 shows the largest correlation slope and the smallest intercept for the GTWR model. It is worth noting that all of the regression line slopes for the four models are less than 1. Figure 5 is present to assess the impact of the numbers of valid observations on the GTWR performance. The R^2 over Hunan (Figure 5a) is smaller than those over Shandong (Figure 5b) and Zhejiang (Figure 5c), due to less observations.

Table 4. Quantitative assessment of model-fitting through ordinary least squares (OLS), geographically weighted regression (GWR), temporally weighted regression (TWR), and GTWR.

Model	R^2	RMSE ($\mu g/m^3$)	MAD ($\mu g/m^3$)	MAPE (%)
OLS	0.45	0.11	12.54	73.24
GWR	0.55	0.10	11.16	61.10
TWR	0.61	0.09	10.59	60.52
GTWR	0.69	0.08	9.38	52.10

Table 5. Quantitative assessment of cross-validation through OLS, GWR, TWR, and GTWR.

Model	R^2	RMSE ($\mu g/m^3$)	MAD ($\mu g/m^3$)	MAPE (%)
OLS	0.44	0.33	12.57	73.45
GWR	0.49	0.31	12.09	68.83
TWR	0.55	0.29	11.27	64.63
GTWR	0.60	0.28	10.68	60.19
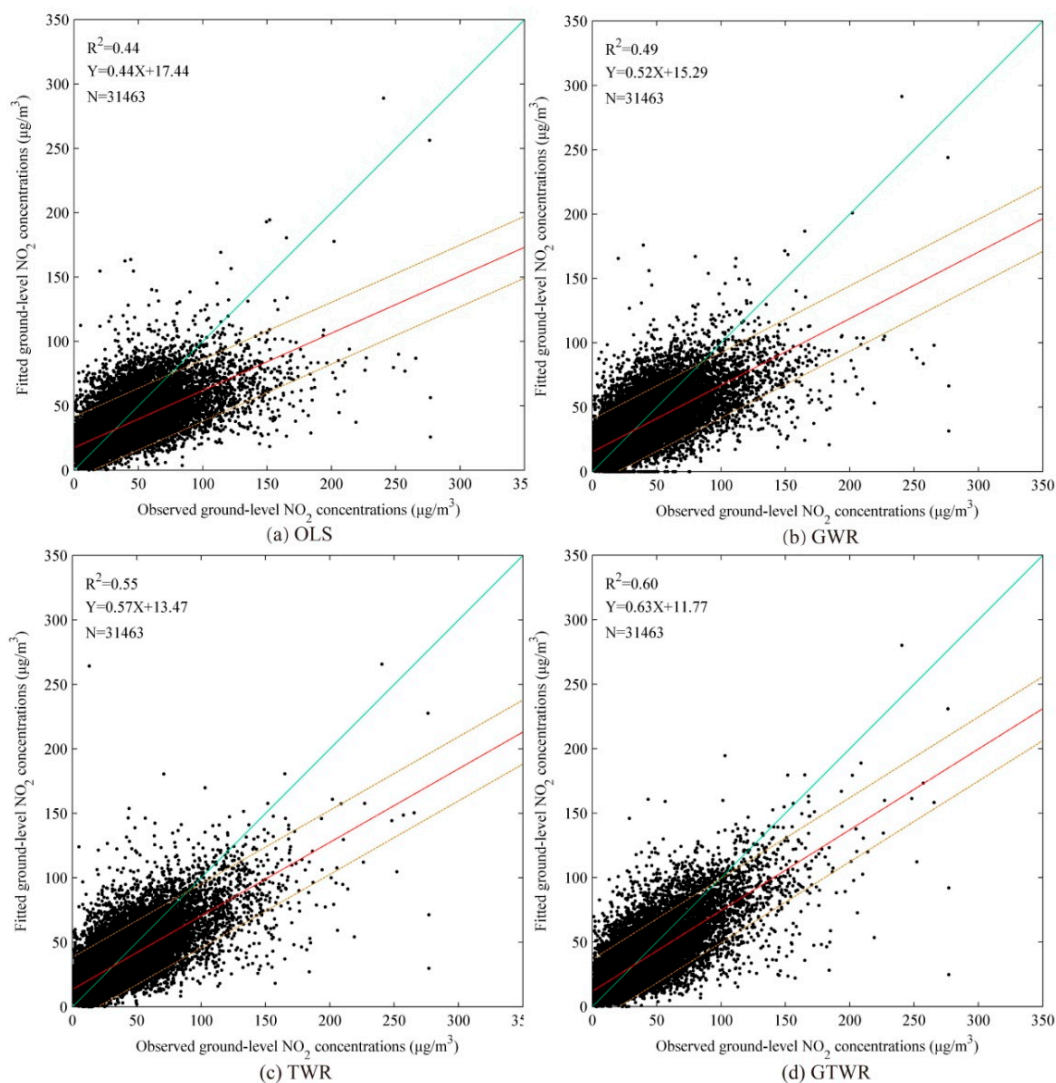
Figure 4. Scatter plots between the observed NO_2 and predicted NO_2 concentrations using OLS (**a**), GWR (**b**), TWR (**c**), and GTWR (**d**) for cross validation over central-eastern China from May 2013 to April 2014.
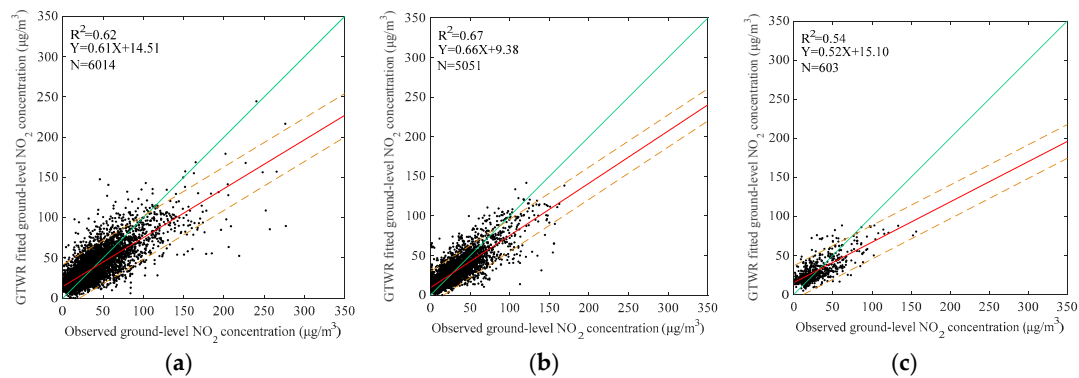
Figure 5. Scatter plots between the observed NO_2 and predicted NO_2 concentrations for cross validation over Shandong (**a**), Zhejiang (**b**), and Hunan (**c**) from May 2013 to April 2014.

There are three possible errors in the estimation of ground level NO_2 concentrations using the satellite-based GTWR model. First, satellite data are collected over an area of hundreds of km^2, while in-situ measurements are point observations. Second, the errors in the retrieval of OMI tropospheric NO_2 columns are underestimated in urban regions and overestimated in remote areas by about -20% and 20%, respectively [38]. Third, the uncertainty in the meteorological parameters can affect the vertical distribution of tropospheric NO_2. Zhang et al. [45] validated the NCEP FNL data against meteorological station data over Henan, China during 2012, and they found the errors of air temperature and pressure are $-3{\sim}2$ K and $-10{\sim}10$ hPa, respectively. We introduced the expected random errors (Gaussian distribution) from the tropospheric NO_2 columns, air temperature, and air pressure, to assess their impact on the performance of the GTWR model. As shown in Table 6 and Figure 6, our model uncertainties are relatively low with the expected uncertainties from the model parameters.
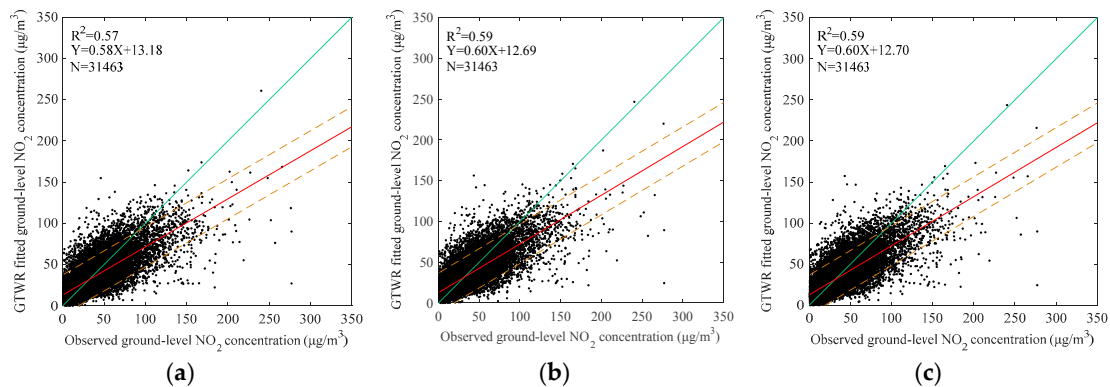

Figure 6. Scatter plots between the observed NO_2 and GTWR predicted NO2 concentrations with random errors from tropospheric NO_2 columns (20%) (**a**), air temperature (2 K) (**b**), and air pressure (10 hPa) (**c**) over central-eastern China from May 2013 to April 2014.

In the GTWR model, the smaller the spatio-temporal distance between two samples is, the greater weight coefficients are given. As illustrated in Figure 7, the GTWR performs much better than the OLS for the samples whose distances to the ambient monitoring stations are within 100 km, whereas the GTWR performance is worse than the OLS (0.41 versus 0.44 for R^2) for the samples that are more than 100 km away from the ambient monitoring stations. In the regions like Anhui, Jiangxi, and Fujian, where the ambient monitoring stations are very sparse and unevenly distributed, the nearest samples are mostly more than 100 km away. Hence, we used adjustable bandwidths according to the sample

distances rather than the fixed ones. As compared to Figure 7, the R^2 in Figure 8 improves from 0.41 to 0.50 for the samples with larger distances (>100 km) after adjusting the bandwidth.

Table 6. Quantitative assessment of GTWR cross-validation with random errors from tropospheric NO_2 columns, air temperature, and air pressure.

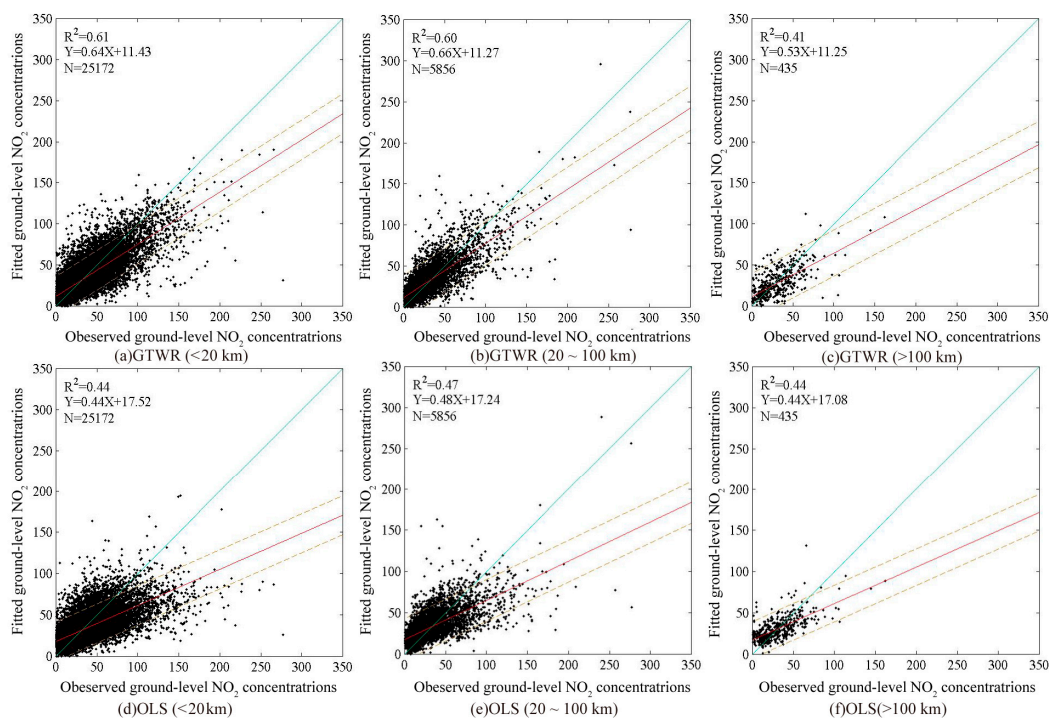| Variations	Random Errors	R^2	RMSE ($\mu g/m^3$)	MAD ($\mu g/m^3$)	MAPE (%)
Tropospheric NO_2 columns	20%	0.57	0.29	11.01	62.40
Air temperature	2 K	0.59	0.28	10.75	61.11
Air pressure	10 hPa	0.59	0.28	10.75	60.86

Figure 7. Scatter plots between the observed NO_2 and predicted NO_2 concentrations using GTWR ((**a**–**c**) and OLS (**d**–**f**) for samples with different distances (**a**,**d**) <20 km; (**b**,**e**) 20–100 km; (**c**,**f**) >100 km) for cross validation over central-eastern China from May 2013 to April 2014.
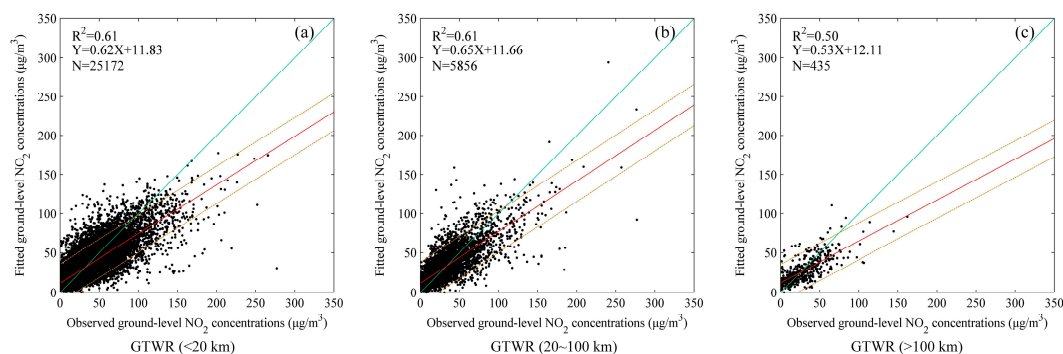

Figure 8. Scatter plots between the observed NO_2 and GTWR predicted NO_2 concentrations for samples with different distances ((**a**) <20 km; (**b**) 20-100 km; (**c**) >100 km) after adjusting the bandwidth for cross validation over central-eastern China from May 2013 to April 2014.

To compare the GTWR method with the chemistry transport model (CTM) approach, we generated the tropospheric NO_2 profiles by using a WRF-Chem model with the monthly MIX Asian anthropogenic emission inventory [46]. This emission inventory has a spatial resolution of $0.25 \times 0.25°$ and involves four emission categories, including industry, power, transport, and residential. The model has 20 vertical levels and the top level pressure is 200 hPa. The RADM2 chemical mechanism is used for the gas-phase chemical reaction calculations. The Modal Aerosol Dynamics Model for Europe-MADE/SORGAM is chosen for the aerosol scheme. Then, we estimated the ground level NO_2 concentrations in January 2014 over central-eastern China using the approach described by Lamsal et al. [18,19]. As shown in Figure 9, the result of the GTWR fitted is much better than the WRF-Chem. Recently, Gu et al. [43] estimated the ground level NO_2 over China using the chemistry transport model approach with the Community Multi-scale Air Quality (CMAQ) model by considering the influence of China's high atmospheric pollution on obtaining the vertical distribution of tropospheric NO_2 profiles. They achieved a correlation coefficient (R) of 0.80 for January 2014, which is comparable to the coefficient of determination (R^2) of 0.60 obtained by the GTWR.
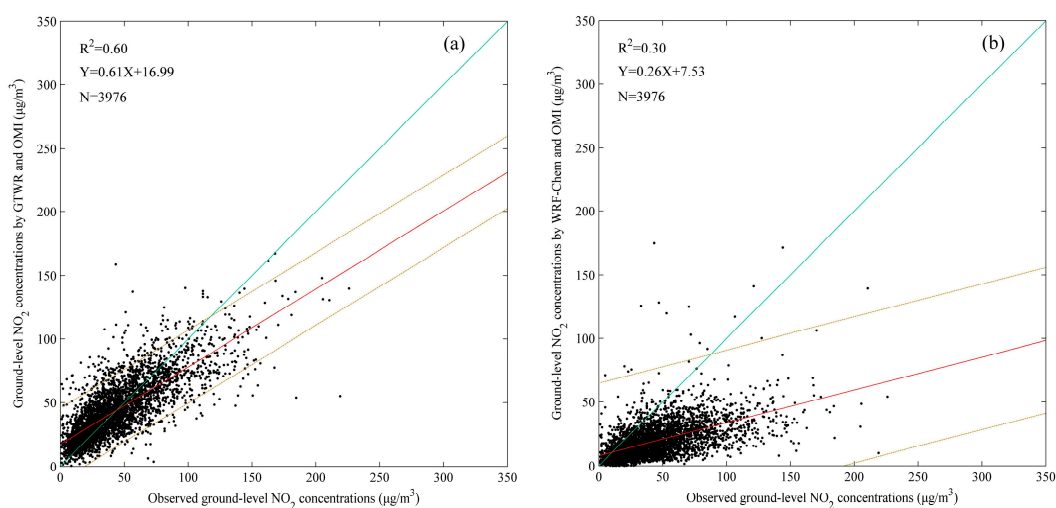

Figure 9. Scatter plots between the observed NO_2 and predicted NO_2 concentrations by GTWR (**a**) and WRF-Chem (**b**) for cross validation over central-eastern China in January 2014.

To further evaluate the performance of the GTWR model, the comparison of the annual mean of NO_2 concentrations between the model-fitted and ground-observed data is given in Figure 10. Overall, the NO_2 concentrations estimated by the GTWR model agree well with the ground-based measurements. More than 90% of the cross-validation stations possess low mean discrepancies of less than 10 $\mu g/m^3$.

4.3. Spatial Distribution of GTWR Fitted Ground-Observed NO_2

The spatial distributions of annual mean NO_2 values are shown in Figure 11. The fitted ground-observed NO_2 concentrations by GTWR in (a) have similar spatial patterns to the satellite tropospheric NO_2 columns in (b). The concentrations are comparable to the interpolated in situ observations using the Kriging method in (c) over the region with high values. Importantly, in the areas without monitoring stations (e.g., southern Jiangxi and northern Fujian), Figure 11a provides more reasonable estimations that are overestimated in Figure 11c. In Figure 11a, high NO_2 concentrations are clustered in the regions of North China Plain, Yangtze River Delta, and Pearl River Delta. Especially, the NO_2 concentrations in southern Hebei, northern Henan, central Shandong, and southern Shaanxi exceeded the Level 2 standard of the Chinese National Ambient Air Quality Standard (40 $\mu g/m^3$). Figure 12 denotes dramatic seasonal changes in the spatial distribution of GTWR fitted ground level NO_2. Unparalleled high values are found in winter, while the lowest values are found in summer.
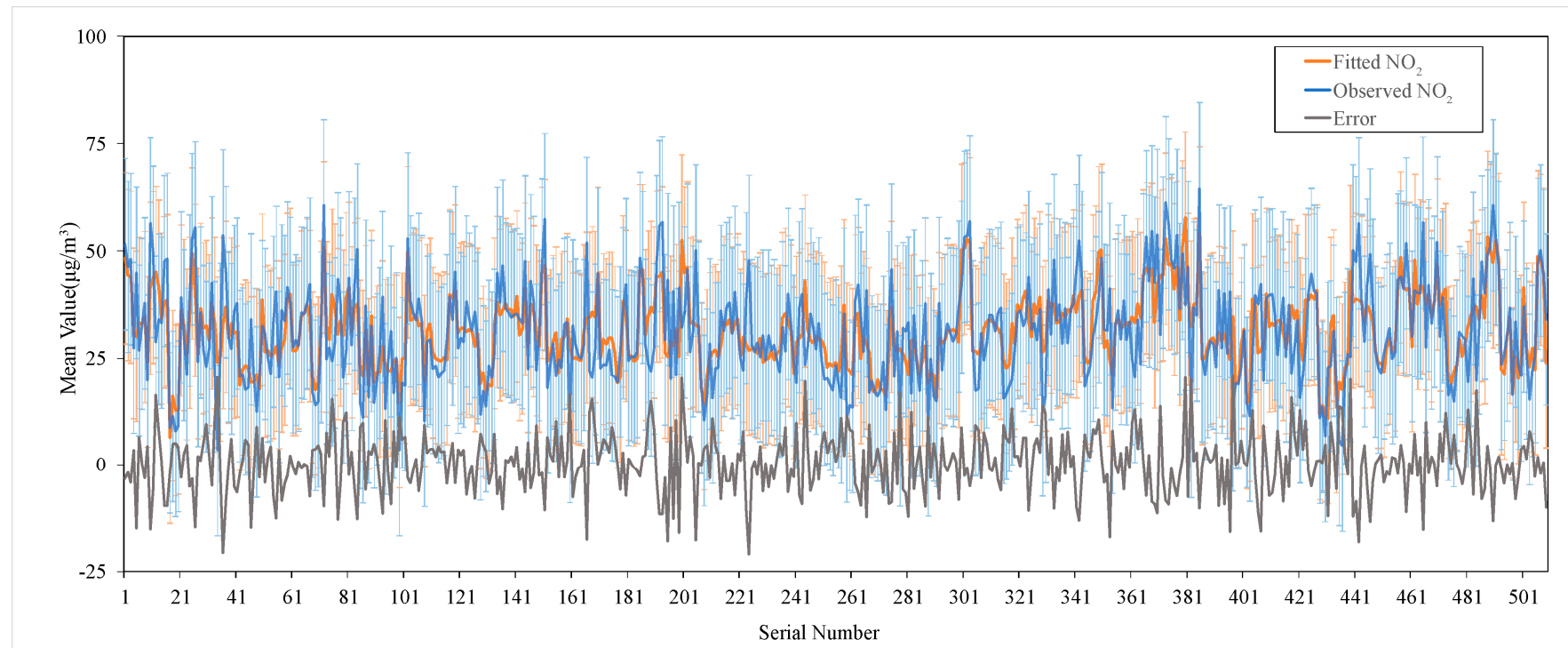
Figure 10. Annual means of observed NO₂ and fitted NO₂ by the GTWR model for all 509 stations.
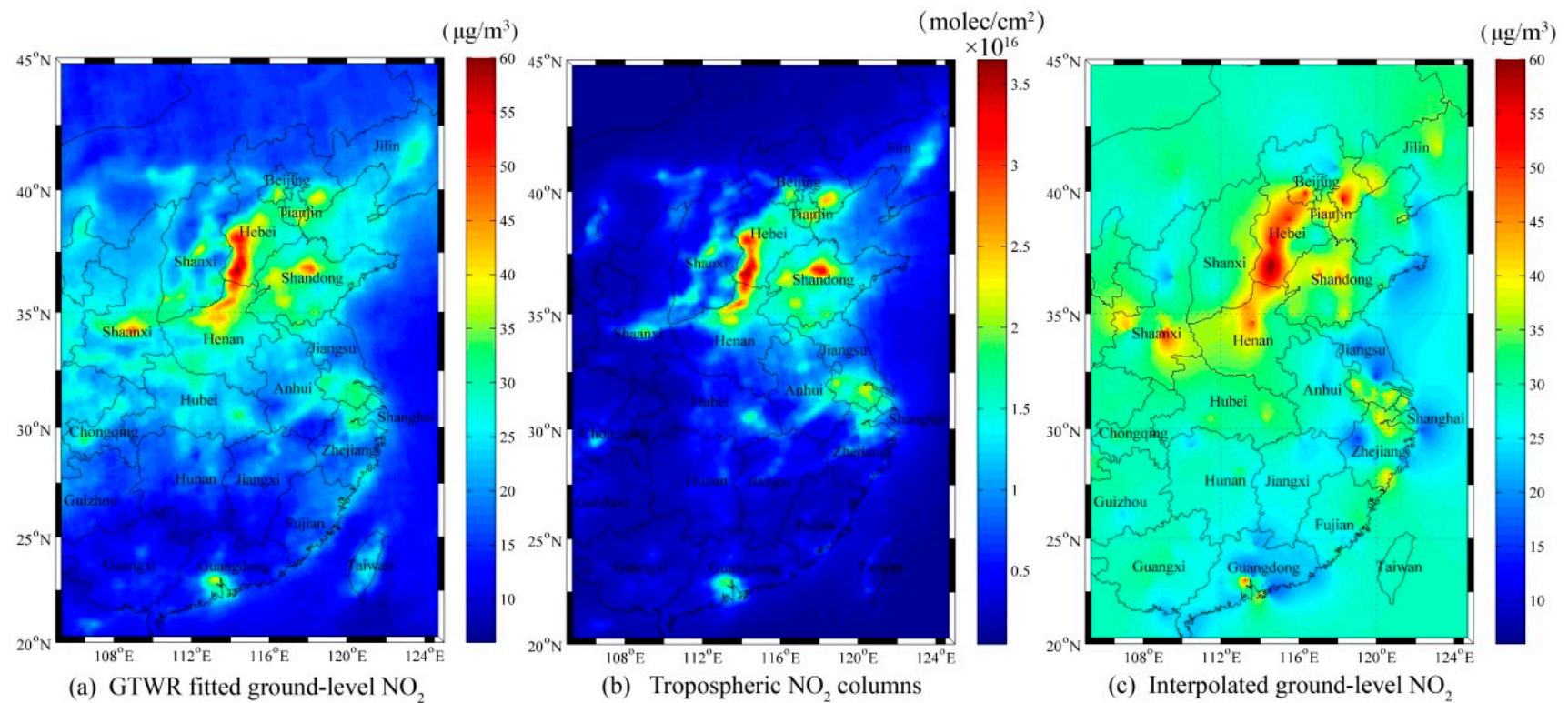
Figure 11. Spatial distribution of annual mean values of (**a**) ground level NO$_2$ concentrations fitted by GTWR model, (**b**) NO$_2$ tropospheric columns, and (**c**) ground level NO$_2$ concentrations interpolated by Kriging method.
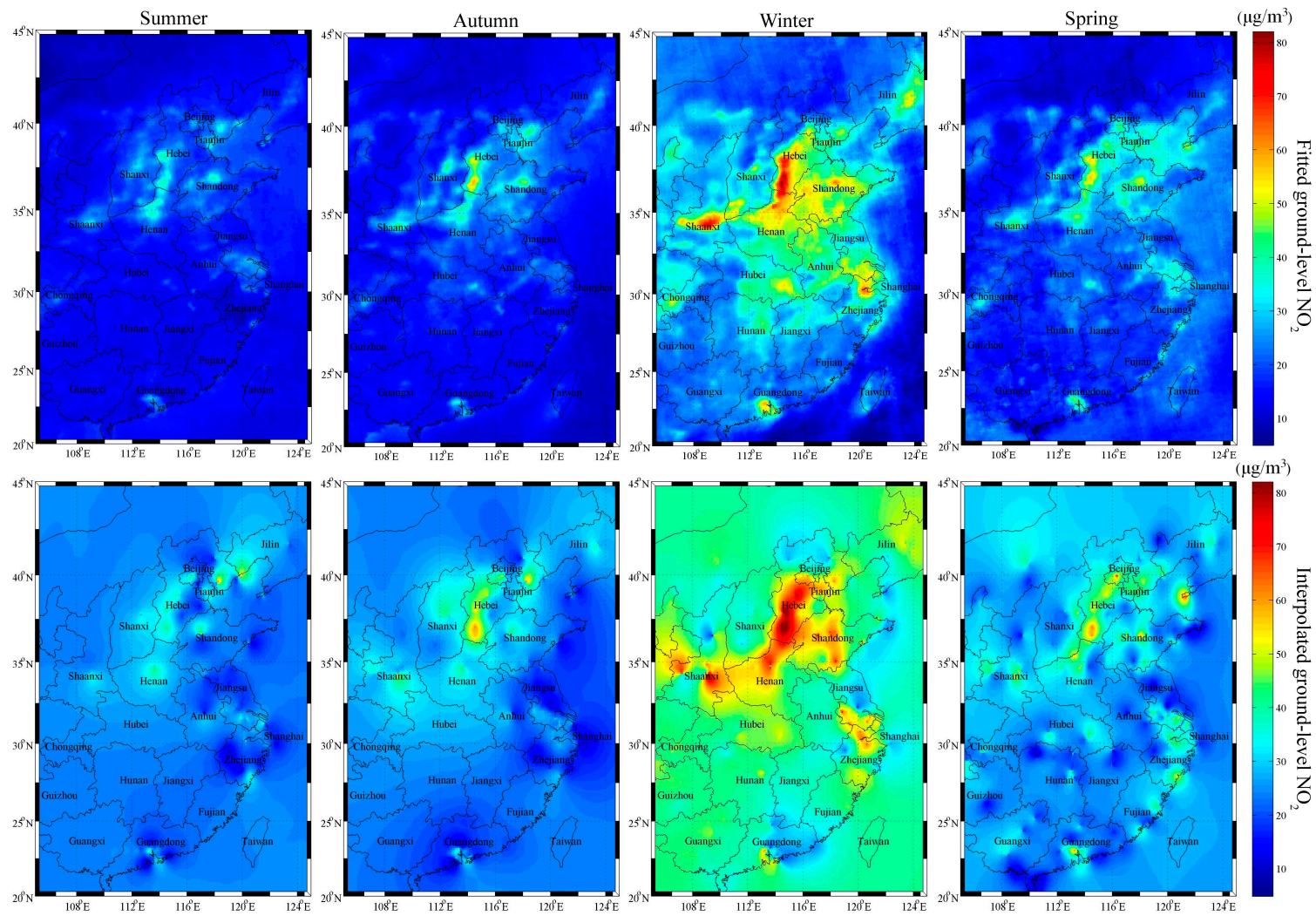
Figure 12. Spatial distribution of seasonal mean values of GTWR fitted (**upper**) and Kriging interpolated (**lower**) ground level NO$_2$ concentrations.

4.4. Population-Weighted Ground Level NO$_2$ Concentrations

Given the NO$_2$ toxicity to human health, it is necessary to evaluate population exposure levels over different provinces. Traditionally, the province-level mean NO$_2$ concentration provided by the Chinese environmental protection agencies are the arithmetic means of all values in administered cities. Here, we calculated the annual mean population-weighted NO$_2$ (AMPNO$_2$) concentrations by using Equation (20). The annual mean NO$_2$ concentrations (AMNO$_2$) and AMPNO$_2$ of 17 provinces in central-eastern China are summarized in Table 7. AMPNO2 is higher than AMNO2 for all of the provinces, especially for densely populated provinces, e.g., Hebei, Beijing, and Guangdong. People from these 17 provinces except Anhui, Fujian, Jiangxi, and Hunan, are exposed to high-level NO$_2$ concentrations (>30 μg/m^3). Heibei, Tianjin, and Beijing suffer from the most serious NO$_2$ pollution, with more than 70% of people affected by high-level NO$_2$. The satellite-estimated ground level NO$_2$ concentration is observed at afternoon (13:00–15:00) leading to underestimated annual mean values.

Table 7. Annual mean NO$_2$ (AMNO$_2$) concentrations and population-weighted NO$_2$ (AMPNO$_2$) concentrations for 17 provinces in central-eastern China.

Province	AMNO$_2$ (μg/m^3)	AMPNO$_2$ (μg/m^3)	Population (Millions)	Proportion of People Exposed to High-Level NO$_2$ Concentrations (>30 μg/m^3)
Hebei	27.47	35.23	108.74	74.14%
Tianjin	31.67	34.38	23.04	85.84%
Beijing	26.09	33.86	33.73	87.03%
Shaanxi	25.66	32.43	53.35	55.78%
Henan	29.73	32.12	132.31	56.30%
Shandong	30.21	31.3	139.65	58.28%
Shanxi	24.59	28.43	54.76	46.07%
Shanghai	26.02	27.87	33.56	14.61%
Jiangsu	24.86	27.04	113.16	35.40%
Hubei	23.4	25.56	81.48	19.49%
Chongqing	22.13	25.29	38.34	21.16%
Zhejiang	21.17	25.08	76.21	21.03%
Anhui	21.8	23.48	84.41	0%
Guangdong	14.91	21.09	138.15	18.92%
Fujian	16.9	18.76	47.94	0%
Jiangxi	15.76	17.23	62.96	0%
Hunan	15.55	16.9	89.44	0%

5. Conclusions

In this study, a satellite-based GTWR model has been applied to estimate ground level NO$_2$ concentrations over central-eastern China. OMI tropospheric NO$_2$ columns, together with ambient monitoring station measurements and meteorological data from May 2013 to April 2014 were considered. The results show that the GTWR model produces the highest cross-validation R^2 (0.60) and the lowest errors (RMSE, MAD, and MAPE), in comparison with other models, i.e., OLS, GWR, and TWR. The model performance is significantly correlated with the meteorological parameters that likely describe the NO$_2$ vertical profile shapes. Our method is better than or comparable to the CTM method.

The satellite-estimated spatial distribution of annual mean NO$_2$ shows a similar spatial pattern to the tropospheric NO$_2$ column and possesses similar value with the in situ observation. High annual mean NO$_2$ concentrations (>40 μg/m^3) are found in southern Hebei, northern Henan, central Shandong, and southern Shaanxi. Seasonal changes in the spatial distribution of ground level NO$_2$ are easily identifiable with unparalleled high values in winter and the lowest values in summer. The population-weighted NO$_2$ demonstrates that people who lived in densely populated areas are more likely to be exposed to high NO$_2$ pollution.

One of the major error sources in the estimation of ground level NO$_2$ concentrations using OMI data is the spatial gradient and the horizontal inhomogeneity between individual satellite pixels. In September 2017, the TROPOMI/S5P will be launched and measure tropospheric NO$_2$ columns with a

higher spatial resolution (7 km $\times$ 7 km) [47], which enables an improved accuracy in the ground level NO_2 estimation.

Author Contributions: Kai Qin, Lanlan Rao, Yang Bai and Jian Xu conceived and designed the experiments; Lanlan Rao, Yang Bai and Kai Qin performed the experiments and analyzed the data; Kai Qin, Lanlan Rao and Yang Bai prepared the manuscript; Jian Xu, Jiaheng Zou, Nan Hao, Shenshen Li and Chao Yu improved the ideas and made revisions.

Conflicts of Interest: The authors declare no conflict of interest.

References

1. Gauderman, W.J.; Gilliland, G.F.; Vora, H.; Avol, E.; Stram, D.; Mcconnell, R.; Thomas, D.; Lurmann, F.; Margolis, H.G.; Rappaport, E.B. Association between air pollution and lung function growth in southern California children. *Am. J. Respir. Crit. Care Med.* **2000**, *162*, 1383–1390. [CrossRef] [PubMed]

2. Chiusolo, M.; Cadum, E.; Stafoggia, M.; Galassi, C.; Berti, G.; Faustini, A.; Bisanti, L.; Vigotti, M.A.; Patrizia, D.M.; Cernigliaro, A. Short-term effects of nitrogen dioxide on mortality and susceptibility factors in 10 Italian cities: The EpiAir study. *Environ. Health Perspect.* **2011**, *119*, 1233. [CrossRef] [PubMed]

3. Stieb, D.M.; Burnett, R.T.; Smithdoiron, M.; Brion, O.; Shin, H.H.; Economou, V. A new multipollutant, no-threshold air quality health index based on short-term associations observed in daily time-series analyses. *J. Air Waste Manag. Assoc.* **2008**, *58*, 435–450. [PubMed]

4. Sioris, C.E.; Kurosu, T.P.; Martin, R.V.; Chance, K. Stratospheric and tropospheric NO_2 observed by SCIAMACHY: First results. *Adv. Space Res.* **2004**, *34*, 780–785. [CrossRef]

5. Boersma, K.F.; Eskes, H.J.; Veefkind, J.P.; Brinksma, E.J.; van der A, R.J.; Sneep, M.; Oord, G.H.J.V.; Levelt, P.F.; Stammes, P.; Gleason, J.F. Near-real time retrieval of tropospheric NO_2 from OMI. *Atmos. Chem. Phys. Discuss.* **2006**, *6*, 12301–12345. [CrossRef]

6. Valks, P.; Pinardi, G.; Richter, A.; Lambert, J.C. Operational total and tropospheric NO_2 column retrieval for GOME-2. *Atmos. Meas. Tech.* **2011**, *4*, 1491. [CrossRef]

7. Irie, H.; Boersma, F.; Kanaya, Y.; Takashima, H.; Xiaole, P.; Wang, Z. Quantitative bias estimates for tropospheric NO_2 columns retrieved from SCIAMACHY, OMI, and GOME-2 using a common standard for East Asia. *Atmos. Meas. Tech.* **2012**, *5*, 2403–2411. [CrossRef]

8. Hassinen, S.; Balis, D.; Bauer, H.; Begoin, M.; Delcloo, A.; Eleftheratos, K.; Gimeno Garcia, S.; Granville, J.; Grossi, M.; Hao, N. Overview of the O3M SAF GOME-2 operational atmospheric composition and UV radiation data products and data availability. *Atmos. Meas. Tech.* **2016**, *9*, 383–407. [CrossRef]

9. Richter, A.; Burrows, J.P.; Nüss, H.; Granier, C.; Niemeier, U. Increase in tropospheric nitrogen dioxide over China observed from space. *Nature* **2005**, *437*, 129–132. [CrossRef] [PubMed]

10. Van Der, A.R.J.; Peters, D.; Eskes, H.; Boersma, K.F.; Roozendael, M.V.; Smedt, I.D.; Kelder, H.M. Detection of the trend and seasonal variation in tropospheric NO_2 over China. *J. Geophys. Res. Atmos.* **2006**, *111*. [CrossRef]

11. Zhang, Q.; Geng, G.N.; Wang, S.W.; Richter, A.; He, K.B. Satellite remote sensing of changes in NOx emissions over China: 1996–2010. *Chin. Sci. Bull.* **2012**, *57*. [CrossRef]

12. Zhang, L.; Lee, C.S.; Zhang, R.; Chen, L. Spatial and temporal evaluation of long term trend (2005–2014) of OMI retrieved NO_2 and SO_2 concentrations in Henan Province, China. *Atmos. Environ.* **2017**, *154*, 151–166. [CrossRef]

13. Liu, F.; Beirle, S.; Zhang, Q.; Dörner, S.; He, K.; Wagner, T. NOx lifetimes and emissions of cities and power plants in polluted background estimated by satellite observations. *Atmos. Chem. Phys.* **2016**, *16*, 5283–5298. [CrossRef]

14. Petritoli, A.; Bonasoni, P.; Giovanelli, G.; Ravegnani, F.; Kostadinov, I.; Bortoli, D.; Weiss, A.; Schaub, D.; Richter, A.; Fortezza, F. First comparison between ground-based and satellite-borne measurements of tropospheric nitrogen dioxide in the Po basin. *J. Geophys. Res. Atmos.* **2004**, *109*. [CrossRef]

15. Vienneau, D.; Hoogh, K.D.; Bechle, M.J.; Beelen, R.; Donkelaar, A.V.; Martin, R.V.; Millet, D.B.; Hoek, G.; Marshall, J.D. Western European land use regression incorporating satellite-and ground-based measurements of NO_2 and PM_{10}. *Environ. Sci. Technol.* **2013**, *47*, 13555–13564. [CrossRef] [PubMed]

16. Lee, H.J.; Koutrakis, P. Daily ambient NO_2 concentration predictions using satellite ozone monitoring instrument NO_2 data and land use regression. *Environ. Sci. Technol.* **2014**, *48*, 2305–2311. [PubMed]

17. Hoek, G.; Eeftens, M.; Beelen, R.; Fischer, P.; Brunekreef, B.; Boersma, K.F.; Veefkind, P. Satellite NO_2 data improve national land use regression models for ambient NO_2 in a small densely populated country. *Atmos. Environ.* **2015**, *105*, 173–180. [CrossRef]

18. Lamsal, L.N.; Martin, R.V.; Donkelaar, A.V.; Steinbacher, M.; Celarier, E.A.; Bucsela, E.; Dunlea, E.J.; Pinto, J.P. Ground level nitrogen dioxide concentrations inferred from the satellite-borne Ozone Monitoring Instrument. *J. Geophys. Res. Atmos.* **2008**, *113*, 280–288. [CrossRef]

19. Lamsal, L.N.; Duncan, B.N.; Yoshida, Y.; Krotkov, N.A.; Pickering, K.E.; Streets, D.G.; Lu, Z. US NO_2 trends (2005–2013): EPA Air Quality System (AQS) data versus improved observations from the Ozone Monitoring Instrument (OMI). *Atmos. Environ.* **2015**, *110*, 0e143. [CrossRef]

20. Kharol, S.K.; Martin, R.V.; Philip, S.; Boys, B.; Lamsal, L.N.; Jerrett, M.; Brauer, M.; Crouse, D.L.; Mclinden, C.; Burnett, R.T. Assessment of the magnitude and recent trends in satellite-derived ground-level nitrogen dioxide over North America. *Atmos. Environ.* **2015**, *118*, 236–245. [CrossRef]

21. Chan, K.L.; Hartl, A.; Lam, Y.F.; Xie, P.H.; Liu, W.Q.; Cheung, H.M.; Lampel, J.; Pöhler, D.; Li, A.; Xu, J. Observations of tropospheric NO_2 using ground based MAX-DOAS and OMI measurements during the Shanghai World Expo 2010. *Atmos. Environ.* **2015**, *119*, 45–58. [CrossRef]

22. Kim, D.; Lee, H.; Hong, H.; Choi, W.; Yun, G.L.; Park, J. Estimation of surface NO_2 volume mixing ratio in four metropolitan cities in Korea using multiple regression models with OMI and AIRS Data. *Remote Sens.* **2017**, *9*, 627. [CrossRef]

23. Song, W.; Jia, H.; Huang, J.; Zhang, Y. A satellite-based geographically weighted regression model for regional $PM_{2.5}$ estimation over the Pearl River Delta region in China. *Remote Sens. Environ.* **2014**, *154*, 1–7. [CrossRef]

24. You, W.; Zang, Z.; Zhang, L.; Li, Z.; Chen, D.; Zhang, G. Estimating ground-level PM_{10} concentration in northwestern China using geographically weighted regression based on satellite AOD combined with CALIPSO and MODIS fire count. *Remote Sens. Environ.* **2015**, *168*, 276–285. [CrossRef]

25. Zou, B.; Pu, Q.; Bilal, M.; Weng, Q.; Zhai, L.; Nichol, J.E. High-resolution satellite mapping of fine particulates based on geographically weighted regression. *IEEE Geosci. Remote Sens. Lett.* **2016**, *13*, 495–499. [CrossRef]

26. You, W.; Zang, Z.; Zhang, L.; Li, Y.; Pan, X.; Wang, W. National-scale estimates of ground-level $PM_{2.5}$ concentration in China using geographically weighted regression based on 3 km resolution MODIS AOD. *Remote Sens.* **2016**, *8*, 184. [CrossRef]

27. Bai, Y.; Wu, L.; Qin, K.; Zhang, Y.; Shen, Y.; Zhou, Y. A geographically and temporally weighted regression model for ground-level $PM_{2.5}$ estimation from satellite-derived 500 m resolution AOD. *Remote Sens.* **2016**, *8*, 262. [CrossRef]

28. Guo, Y.; Tang, Q.; Gong, D.Y.; Zhang, Z. Estimating ground-level $PM_{2.5}$ concentrations in Beijing using a satellite-based geographically and temporally weighted regression model. *Remote Sens. Environ.* **2017**, *198*, 140–149. [CrossRef]

29. Levelt, P.F.; Oord, G.H.J.V.; Dobber, M.R.; Malkki, A.; Visser, H.; Vries, J.D.; Stammes, P.; Lundell, J.O.V.; Saari, H. The ozone monitoring instrument. *IEEE Trans. Geosci. Remote Sens.* **2006**, *44*, 1093–1101. [CrossRef]

30. Platt, U.; Stutz, J. Differential Absorption Spectroscopy. In *Differential Optical Absorption Spectroscopy*; Springer: Berlin/Heidelberg, Germany, 2008; pp. 135–174.

31. Bucsela, E.J.; Krotkov, N.A.; Celarier, E.A.; Lamsal, L.N. A new stratospheric and tropospheric NO2 retrieval algorithm for nadir-viewing satellite instruments: Applications to OMI. *Atmos. Meas. Tech.* **2013**, *6*, 2607. [CrossRef]

32. Douglass, A.R.; Stolarski, R.S.; Strahan, S.E.; Connell, P.S. Radicals and reservoirs in the GMI chemistry and transport model: Comparison to measurements. *J. Geophys. Res. Atmos.* **2004**, *109*. [CrossRef]

33. Bucsela, E.J.; Celarier, E.A.; Gleason, J.L.; Krotkov, N.A.; Lamsal, L.N.; Marchenko, S.V.; Swartz, W.H. OMNO2 Readme Document Data Product Version 3.0. 2016. Available online: https://aura.gesdisc.eosdis.nasa.gov/data//Aura_OMI_Level2/OMNO2.003/doc/README.OMNO2.pdf (accessed on 16 September 2016).

34. Boersma, K.F.; Eskes, H.J.; Brinksma, E.J. Error analysis for tropospheric NO_2 retrieval from space. *J. Geophys. Res. Atmos.* **2004**, *109*. [CrossRef]

35. Boersma, F.; Dirksen, R.; Brunner, D.; Zhou, Y.; Huijnen, V.; Eskes, H.; Veefkind, P.; Kleipool, Q.; Dobber, M.; Stammes, P. An improved retrieval of tropospheric NO2 columns from the Ozone Monitoring Instrument. *Atmos. Meas. Tech.* **2011**, *4*, 1905–1928. [CrossRef]

36. Hong, H.; Lee, H.; Kim, J.; Jeong, U.; Ryu, J.; Lee, D.S. Investigation of simultaneous effects of aerosol properties and aerosol peak height on the air mass factors for space-borne NO_2 retrievals. *Remote Sens.* **2017**, *9*, 208. [CrossRef]

37. Wang, Y.; Beirle, S.; Lampel, J.; Koukouli, M.; De Smedt, I.; Theys, N.; Li, A.; Wu, D.; Xie, P.; Liu, C. Validation of OMI, GOME-2A and GOME-2B tropospheric NO_2, SO_2 and HCHO products using MAX-DOAS observations from 2011 to 2014 in Wuxi, China: Investigation of the effects of priori profiles and aerosols on the satellite products. *Atmos. Chem. Phys.* **2017**, *17*, 5007. [CrossRef]

38. Lamsal, L.N.; Krotkov, N.A.; Celarier, E.A.; Swartz, W.H.; Pickering, K.E.; Bucsela, E.J.; Martin, R.V.; Philip, S.; Irie, H.; Cede, A. Evaluation of OMI operational standard NO_2 column retrievals using in situ and surface-based NO_2 observations. *Atmos. Chem. Phys.* **2014**, *14*, 11587–11609. [CrossRef]

39. Wang, S.; Zhang, Q.; Martin, R.V.; Philip, S.; Liu, F.; Li, M.; Jiang, X.; He, K. Satellite measurements oversee China's sulfur dioxide emission reductions from coal-fired power plants. *Environ. Res. Lett.* **2015**, *10*, 114015. [CrossRef]

40. Huang, B.; Wu, B.; Barry, M. Geographically and temporally weighted regression for modeling spatio-temporal variation in house prices. *Int. J. Geogr. Inf. Sci.* **2010**, *24*, 383–401. [CrossRef]

41. Beelen, R.; Hoek, G.; Pebesma, E.; Vienneau, D.; Hoogh, K.D.; Briggs, D.J. Mapping of background air pollution at a fine spatial scale across the European union. *Sci. Total Environ.* **2009**, *407*, 1852–1867. [CrossRef] [PubMed]

42. Young, M.T.; Bechle, M.J.; Sampson, P.D.; Szpiro, A.A.; Marshall, J.D.; Sheppard, L.; Kaufman, J.D. Satellite-based NO_2 and model validation in a national prediction model based on universal Kriging and land-use regression. *Environ. Sci. Technol.* **2016**, *50*, 3686–3694. [CrossRef] [PubMed]

43. Gu, J.; Chen, L.; Yu, C.; Li, S.; Tao, J.; Fan, M.; Xiong, X.; Wang, Z.; Shang, H.; Su, L. Ground-level NO2 concentrations over China inferred from the Satellite OMI and CMAQ Model simulations. *Remote Sens.* **2017**, *9*, 519. [CrossRef]

44. Ma, J.Z.; Beirle, S.; Jin, J.L.; Shaiganfar, R.; Yan, P.; Wagner, T. Tropospheric NO_2 vertical column densities over Beijing: Results of the first three years of ground-based MAX-DOAS measurements (2008–2011) and satellite validation. *Atmos. Chem. Phys.* **2013**, *13*, 1547–1567. [CrossRef]

45. Zhang, Y.T.; Chen, Y.D. Error comparison analysis between FNL data and observation data of air temperature, air pressure and ground temperature in Henan Province in 2012. *Meteorol. Environ. Sci.* **2014**, *37*, 93–97. (In Chinese)

46. Li, M.; Zhang, Q.; Kurokawa, J.; Woo, J.H.; He, K.; Lu, Z.; Ohara, T.; Song, Y.; Streets, D.G.; Carmichael, G.R. MIX: A mosaic Asian anthropogenic emission inventory under the international collaboration framework of the MICS-Asia and HTAP. *Atmos. Chem. Phys.* **2017**, *17*, 935. [CrossRef]

47. Veefkind, J.P.; Aben, I.; Mcmullan, K.; Förster, H.; Vries, J.D.; Otter, G.; Claas, J.; Eskes, H.J.; Haan, J.F.D.; Kleipool, Q. TROPOMI on the ESA Sentinel-5 Precursor: A GMES mission for global observations of the atmospheric composition for climate, air quality and ozone layer applications. *Remote Sens. Environ.* **2012**, *120*, 70–83. [CrossRef]